

# Why is El Niño warm?

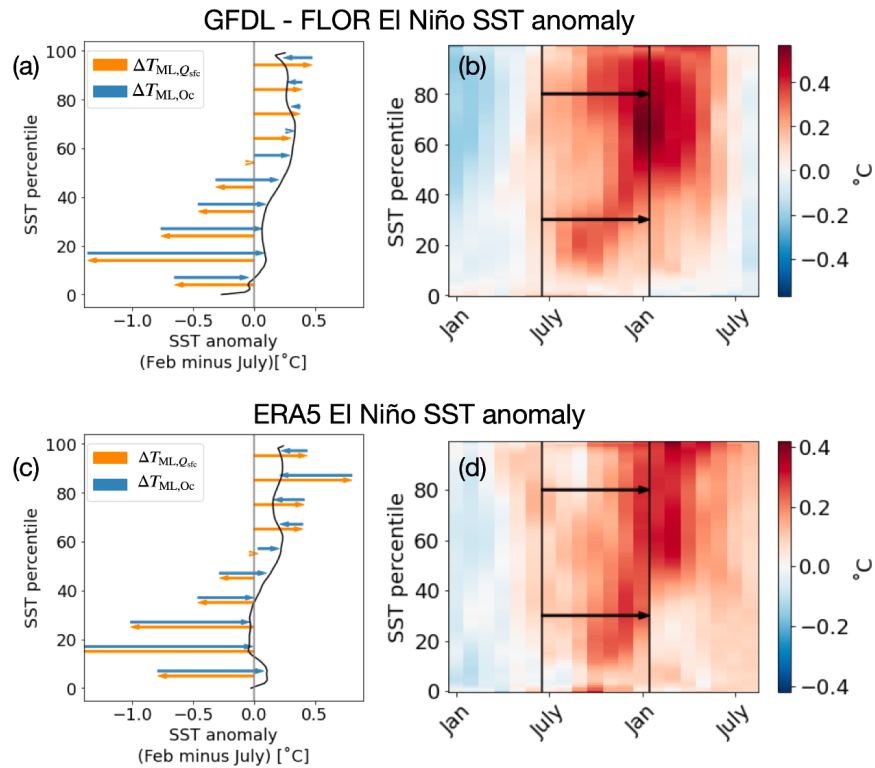
Allison Hogikyan<sup>1</sup>, Laure Resplandy<sup>1</sup>, and Stephan Fueglistaler<sup>1</sup>

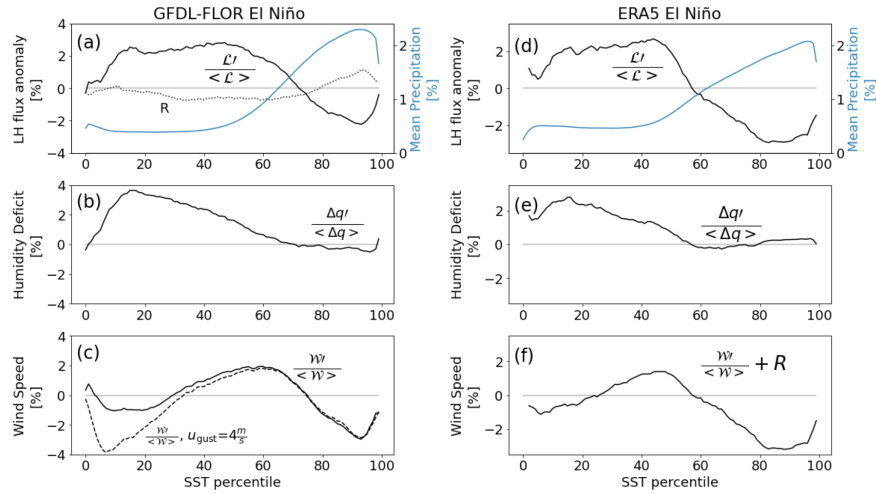
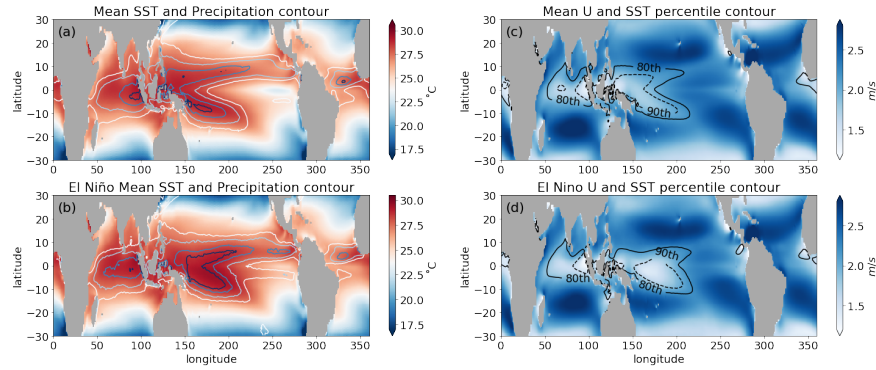
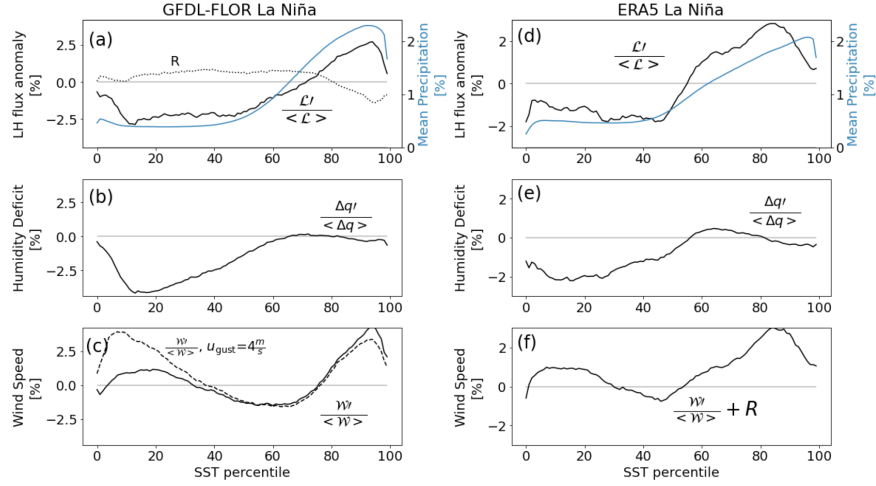
<sup>1</sup>Princeton University

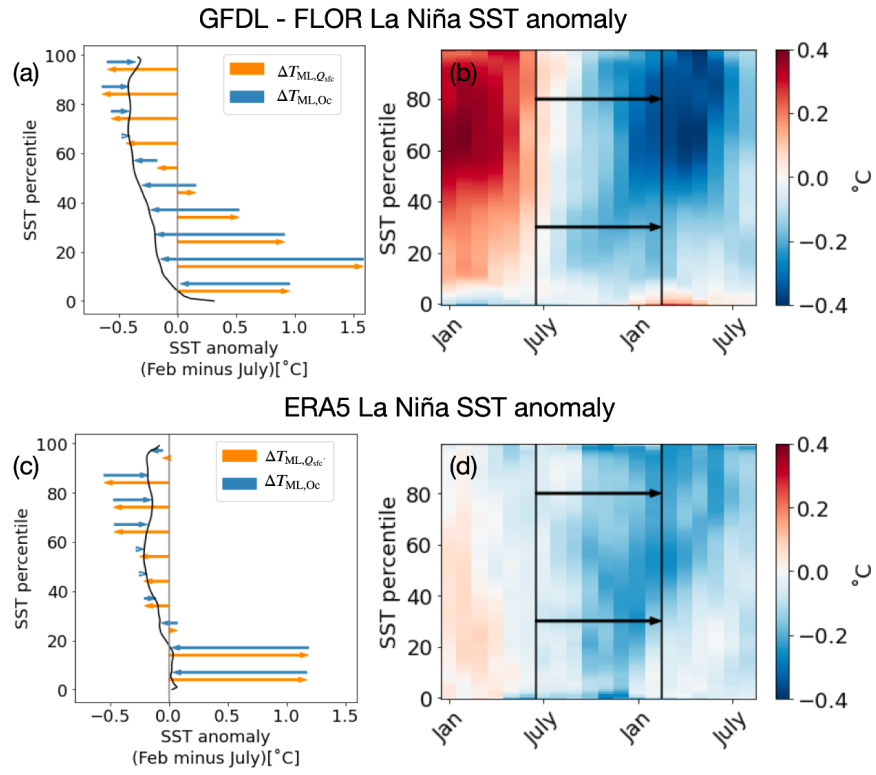
November 24, 2022

## Abstract

The geographic rearrangement of the tropical oceanic and atmospheric circulation during an El Niño event is associated with a well-understood strong surface warming of the climatologically cold eastern equatorial Pacific. However, the concomitant warming of the warmest waters where deep convection occurs - responsible for the tropics-wide free tropospheric warming- is less well understood. Here, we show that in both a coupled atmosphere-ocean climate model and in reanalysis data, El Niño is associated with an increase in evaporation over the colder ~70%, but with a decrease in evaporation over the warmest ~30% of the tropical oceans where atmospheric deep convection connects the surface with the free troposphere. The reduction in evaporation is driven by a weakening of the near-surface winds. We propose that the prominent tropics-wide warming during El Niño is a consequence of the reduction of near-surface winds in regions of deep convection due to the anomalous large-scale circulation.







# Why is El Niño warm?

Allison K. Hogikyan<sup>1\*</sup>, Laure Resplandy<sup>2,3</sup>, Stephan Fueglistaler<sup>1,2</sup>,

<sup>1</sup>Princeton University, Atmospheric and Oceanic Sciences Program

<sup>2</sup>Princeton University Department of Geosciences

<sup>3</sup>Princeton University High Meadows Environmental Institute

## Key Points:

- Tropics-wide warming during El Niño due to warming of the warm ocean regions with deep convection
- The warming of warm regions results from a decrease in evaporation driven by surface winds
- Anomalous atmospheric large-scale circulation leads to wind decrease and explains prominent warming

---

\*Current address, 300 Forrester Road, Sayre Hall, Princeton NJ 08540

Corresponding author: A. K. Hogikyan, [hogikyan@princeton.edu](mailto:hogikyan@princeton.edu)

**Abstract**

The geographic rearrangement of the tropical oceanic and atmospheric circulation during an El Niño event is associated with a well-understood strong surface warming of the climatologically cold eastern equatorial Pacific. However, the concomitant warming of the warmest waters where deep convection occurs - responsible for the tropics-wide free tropospheric warming- is less well understood. Here, we show that in both a coupled atmosphere-ocean climate model and in reanalysis data, El Niño is associated with an increase in evaporation over the colder  $\sim 70\%$ , but with a decrease in evaporation over the warmest  $\sim 30\%$  of the tropical oceans where atmospheric deep convection connects the surface with the free troposphere. The reduction in evaporation is driven by a weakening of the near-surface winds. We propose that the prominent tropics-wide warming during El Niño is a consequence of the reduction of near-surface winds in regions of deep convection due to the anomalous large-scale circulation.

**Plain Language Summary**

El Niño events are associated with a well-understood strong surface warming of the climatologically cold eastern equatorial Pacific and a less-well understood increase in global-mean surface and atmospheric temperatures. The warming of the warmest waters where atmospheric deep convection occurs is responsible for the tropics-wide free tropospheric warming, which is the first step in communicating the warm anomaly beyond the equatorial Pacific. We find that a decrease in surface wind speed, tied to the weakening of the Walker circulation, controls the surface energy budget and warming of these regions.

**1 Introduction**

The El Niño/Southern Oscillation (ENSO) is the largest source of natural variability in the climate system and strongly modulates global atmospheric and surface temperatures. Warm ENSO events, El Niño events, are characterized by a slowing of the wind-driven upwelling of cold water in the eastern equatorial Pacific. This causes the sea surface temperature (SST) to increase in this otherwise cold tropical region (Bjerknes, 1969; S. G. H. Philander, 1983). This ocean-forced positive SST anomaly increases local evaporation, acting as a negative feedback that moderates the surface warming in this region (Trenberth, 2002; W. Wang & McPhaden, 2000).

43 El Niño events are identified and their strength quantified by the warming in the  
44 east Pacific (Trenberth, 1997), but their impact is global, communicated through a warm-  
45 ing of the tropical free troposphere and geographical rearrangement of atmospheric con-  
46 vection (Rasmusson & Wallace, 1983; Lintner & Chiang, 2005; Seager et al., 2003; Chi-  
47 ang & Sobel, 2002; Klein et al., 1999; Yulaeva & Wallace, 1994; Alexander et al., 2002;  
48 Lau & Nath, 1996). The rearrangement of convection (Figure 1a, b) weakens the Walker  
49 circulation (e.g. S. G. H. Philander (1983)), strengthens the zonal-mean Hadley circu-  
50 lation (Lu et al., 2008; Seager et al., 2003), and induces a planetary wave that affects  
51 extratropical weather patterns (Rasmusson & Wallace, 1983). Both the weakening of the  
52 Walker cell and the warming of the free troposphere can affect SSTs in the tropical At-  
53 lantic and Indian Oceans (Chiang & Sobel, 2002; Lohmann & Latif, 2007). This tropics-  
54 wide, and eventually global, warming during El Niño events primarily results from the  
55 warming of the warmest regions of the tropical oceans where atmospheric deep convec-  
56 tion connects the surface and the free troposphere (e.g. Sobel et al. (2002); Brown and  
57 Bretherton (1997)). Thus, in order to understand the prominent tropics-wide warming  
58 signal during El Niño, one must ask what processes allow the SSTs in the warmest re-  
59 gions to increase.

60 It is recognized that the surface energy budget of the warmest regions, where the  
61 thermocline is deep, can be strongly affected by changes in evaporation driven by sur-  
62 face wind anomalies associated with the response of the Walker circulation to ENSO.  
63 Specifically, part of the eastward shift of the local SST maximum during El Niño has been  
64 attributed to the change in the zonal structure of the zonal wind over the warm pool (B. Wang,  
65 1995). Here, we argue that the change in the zonal wind not only leads to the eastward  
66 displacement of the local SST maximum, but is also responsible for the tropical aver-  
67 age warming during El Niño relative to the climatological base state.

68 We use a pre-industrial control experiment in a coupled atmosphere-ocean global  
69 climate model (GCM) and the fifth-generation ECMWF Reanalysis (ERA5), a recon-  
70 struction of the climate state over the period 1979-2019. In the colder parts of the trop-  
71 ical oceans, evaporation increases when the surface warms. This negative feedback is the  
72 expected response of the surface energy budget to the reduced upwelling of cold waters  
73 (Trenberth, 2002; W. Wang & McPhaden, 2000; Lloyd et al., 2011). Conversely, we find  
74 that evaporation decreases in the warm regions where atmospheric deep convection oc-  
75 curs. This decrease in evaporation is associated with a decrease in surface wind speed.

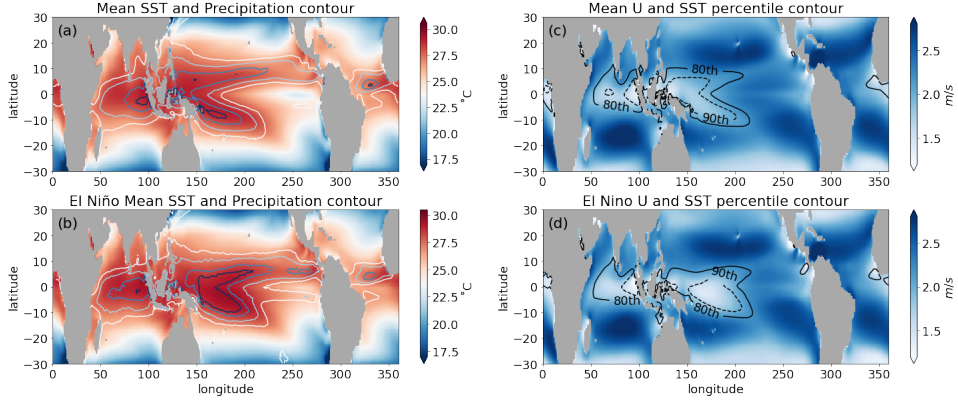


**Figure 1.** Mean and El Niño SST and surface winds in GFDL-FLOR (a, b) SST with contours of precipitation intensity simulated by GFDL-FLOR preindustrial control experiment. Darker blue contours represent more intense precipitation. (c, d) The simulated near-surface wind speed with contours of 80<sup>th</sup> (solid) and 90<sup>th</sup> (dashed) percentiles of SST. The wind speed shown only includes winds resolved on the model grid ( $U = \sqrt{u^2 + v^2}$ ). The lower row (panels b, d) only includes months in the experiment when the normalized Niño3.4 index exceeds 0.6.

76 We therefore propose that the anomalous large-scale circulation leads to the prominent  
 77 tropics-wide warming by decreasing near-surface wind speeds over the sea surface where  
 78 convection occurs. The resulting decrease in evaporation leads to the surface warming,  
 79 which atmospheric convection then communicates to the free troposphere.

## 80 2 Data and Methods

### 81 2.1 GFDL-FLOR coupled model

82 We analyze the behavior of ENSO in the Forecast Oriented Low Ocean Resolution  
 83 configuration of the Geophysical Fluid Dynamics Laboratory (GFDL) coupled climate  
 84 model, referred to as FLOR (Vecchi et al., 2014). This model uses the nominal 1° res-  
 85 olution ocean and sea ice model from GFDL-CM2.1 (Delworth et al., 2006) but a higher  
 86 resolution (0.5°) atmosphere from the GFDL-CM2.5 (Delworth et al., 2012) model and  
 87 an improved land model (LM3, (Milly et al., 2014)). The ocean resolution telescopes to  
 88 0.333° meridional spacing near the equator. We use 100 years of FLOR results from a  
 89 pre-industrial control experiment, in which atmospheric CO<sub>2</sub> concentrations, aerosol and  
 90 solar forcing are prescribed at 1860 levels (Yang et al., 2019).

## 91 2.2 ECMWF Reanalysis

92 We also use data from the European Centre for Medium-Range Weather Forecasts  
 93 (ECMWF) reanalysis (ERA5), a reconstruction of the climate state since 1979. ERA5  
 94 assimilates historical observations onto a global 30km grid (Hersbach et al., 2019). Long-  
 95 term linear trends are removed at each location. We analyze the time period January  
 96 1979 to February 2019, which includes seven El Niño events (1982-83, 1986-87, 1991-92,  
 97 1997-98, 2002-03, 2009-10, 2014-15).

## 98 2.3 SST Percentiles

99 In order to differentiate the behavior at warm and cold SSTs without imposing a  
 100 temperature or precipitation threshold, we organize surface (2D) fields by SST. After sort-  
 101 ing the tropical (30°S:30°N) SSTs from coldest (0th percentile) to warmest (100th per-  
 102 centile), we average each variable into one hundred equal-area bins, which we refer to  
 103 as SST percentiles.

## 104 2.4 Oceanic Mixed Layer Heat Budget

105 A simple mixed layer budget reveals the importance of surface heat fluxes for the  
 106 warm anomaly at the highest SSTs. A change in mixed layer temperature  $T_{ML}$  over a  
 107 time interval (in this case, the anomalous surface warming during El Niño) results from  
 108 either the surface heat flux ( $Q_{sfc}$ ) or oceanic advection and mixing, as denoted below.

$$\int_{t_1}^{t_2} dT_{ML,Q_{sfc}} + dT_{ML,Oc} = \Delta T_{ML,Q_{sfc}} + \Delta T_{ML,Oc} = \Delta T_{ML} \approx \Delta SST \quad (1)$$

109 where  $dT_{ML,Q_{sfc}} = \frac{Q_{sfc}}{\rho c_p H_{ML}} \partial t$ ,  $Q_{sfc}$  is defined as the net radiative, latent and sen-  
 110 sible fluxes at the air-sea interface ( $Q_{sfc} = \mathcal{R}_{dn} - \mathcal{R}_{up} - \mathcal{L} - \mathcal{S}$ ),  $t$  is time,  $\rho$  is the den-  
 111 sity of seawater,  $c_p$  is the heat capacity of seawater, and  $H_{ML}$  is the depth of the mixed  
 112 layer, defined as the depth where the density is  $0.03 \frac{\text{kg}}{\text{m}^3}$  greater than at the surface. We  
 113 estimate the temperature change due to ocean processes  $dT_{ML,Oc}$  as a residual from Equa-  
 114 tion 1. Note that  $T_{ML}$  approximates the SST very closely.

115 To account for the anomalous SST increase during El Niño events, we remove the  
 116 monthly-mean seasonal cycle and then integrate the anomalous ocean and surface forc-  
 117 ings during the growth phase of each event. The growth phase is defined to be between  
 118 the month of July, when the Niño 3.4 index first becomes positive, and the month of Jan-

119 uary, after the peak of the index (Figure 2). The integrated forcings during this time pe-  
 120 riod approximately account for the SST increase from the beginning of July to the be-  
 121 ginning of February.

## 122 2.5 Controls on Latent Heat Flux

123 The latent heat flux  $\mathcal{L}$  is proportional to the surface moisture deficit  $\Delta q$ , the sur-  
 124 face wind speed  $W$ , and properties of the air-sea interface according to the bulk formula  
 125 for evaporation:

$$\mathcal{L} = L \cdot C_E \cdot \rho_a \cdot W \cdot \Delta q \quad (2)$$

126  $L$  is the specific latent heat of evaporation,  $C_E$  is the bulk transfer coefficient for evap-  
 127 oration,  $\rho_a$  is the density of the near-surface air,  $\Delta q = q_{\text{sfc}}^* - q_{2\text{m}}$ , the difference be-  
 128 tween the saturation specific humidity at SST and the near surface (2 meter) humidity,  
 129 and  $W$  is the wind speed at the surface (Large & Yeager, 2009). We find that variations  
 130 in  $\mathcal{L}$  are dominated by changes in  $W$  and  $\Delta q$ , and write:

$$\frac{\mathcal{L}'}{\langle \mathcal{L} \rangle} = \frac{W'}{\langle W \rangle} + \frac{\Delta q'}{\langle \Delta q \rangle} + R \quad (3)$$

131 where  $R$  is the residual and all terms are monthly means. Primes ( $X'$ ) represent  
 132 anomalies from the seasonal cycle while brackets ( $\langle X \rangle$ ) are the climatological monthly  
 133 mean values of the variable  $X$ . We take the latent heat flux to be positive when it is from  
 134 the ocean to the atmosphere.  $R$  includes variations in  $C_E$  and  $\rho_a$  as well as covariation  
 135 on sub-monthly time scales of the wind speed and humidity deficit. It is small relative  
 136 to the other terms (Figure 3a) and we do not discuss it further.

137 We use slightly different methods to calculate  $\Delta q$  from the ERA5 and GFDL-FLOR  
 138 data. In both cases,  $q_{\text{sfc}}^*$  is calculated from the SST. We use the two meter relative hu-  
 139 midity and  $q_{\text{sfc}}^*$  to calculate  $q_{2\text{m}}$  from GFDL-FLOR, whereas in ERA5,  $q_{2\text{m}}$  is calculated  
 140 from the two meter dewpoint temperature. We utilize additional information about the  
 141 calculation of  $W$  in GFDL-FLOR in Section 3.2.

## 142 3 Results

### 143 3.1 Air-sea heat flux warms the warmest SSTs

144 Figure 2 shows the average evolution of the SST anomaly during an El Niño event.  
 145 Tropical SSTs are sorted from coldest to warmest in what we call SST percentiles (See

146 Methods). While certain regions may warm (e.g. east Pacific) or cool (e.g. west Pacific),  
147 sorting into SST bins makes it clear that all percentiles warm (see also Sobel et al. (2002);  
148 Fueglistaler (2019)).

149 In order to identify which are the ‘warmest SSTs’ relevant for variations in free tro-  
150 pospheric temperature, we identify where convection is concentrated in SST percentiles.  
151 With precipitation as a proxy, it is clear that convection is largely confined to the warmest  
152 30% of the tropics (Figure 3a). This is also the area with SSTs equal or higher than about  
153 27°C, the well-known approximate threshold for deep convection in the current climate  
154 (Graham & Barnett, 1987).

155 In both GFDL-FLOR and ERA5, the surface warming of cold percentiles (0-60 per-  
156 centiles) is attributed to oceanic forcing (advection and mixing), while surface heat fluxes  
157 have a cooling effect that partially offsets the oceanic influence (Figure 2a,c). The SST  
158 anomaly in low and middle percentiles begins to emerge in boreal fall prior to the peak  
159 of the event (Figure 2b,d). As the surface warms, the evaporation rate increases so that  
160  $Q_{\text{sfc}}$  opposes the surface warming (W. Wang & McPhaden, 2000; Lloyd et al., 2011). This  
161 is consistent with the expectation that the signal seen in colder percentile bins should  
162 be associated with the decrease in the Pacific upwelling and vertical mixing. The SST  
163 anomaly in the cold percentiles in Figure 2(a, c) is small compared to the warming of  
164 the upwelling region in the equatorial Eastern Pacific. This is largely due to the fact that  
165 this region is relatively small and other regions may not or only weakly warm due to other  
166 processes (Chiang & Sobel, 2002; Lintner & Chiang, 2005; Klein et al., 1999). Thus, the  
167 strong warming in this region primarily leads to a shuffling in rank in percentile space.  
168 The peak warming at the warmest SSTs (70-100 percentiles) is in February-March, af-  
169 ter that of the colder SSTs (Figure 2b,d). Since the Niño3.4 index is based on SST anoma-  
170 lies at the cold SSTs, the El Niño warm anomaly in warm percentiles peaks later than  
171 the Niño3.4 index. Consistent with our expectation that the warmest SSTs determine  
172 the temperature of the tropical troposphere, the peak in the warm anomaly in the trop-  
173 ical troposphere is also delayed from that of the Niño3.4 index (Sobel et al., 2002; Fueglistaler,  
174 2019).

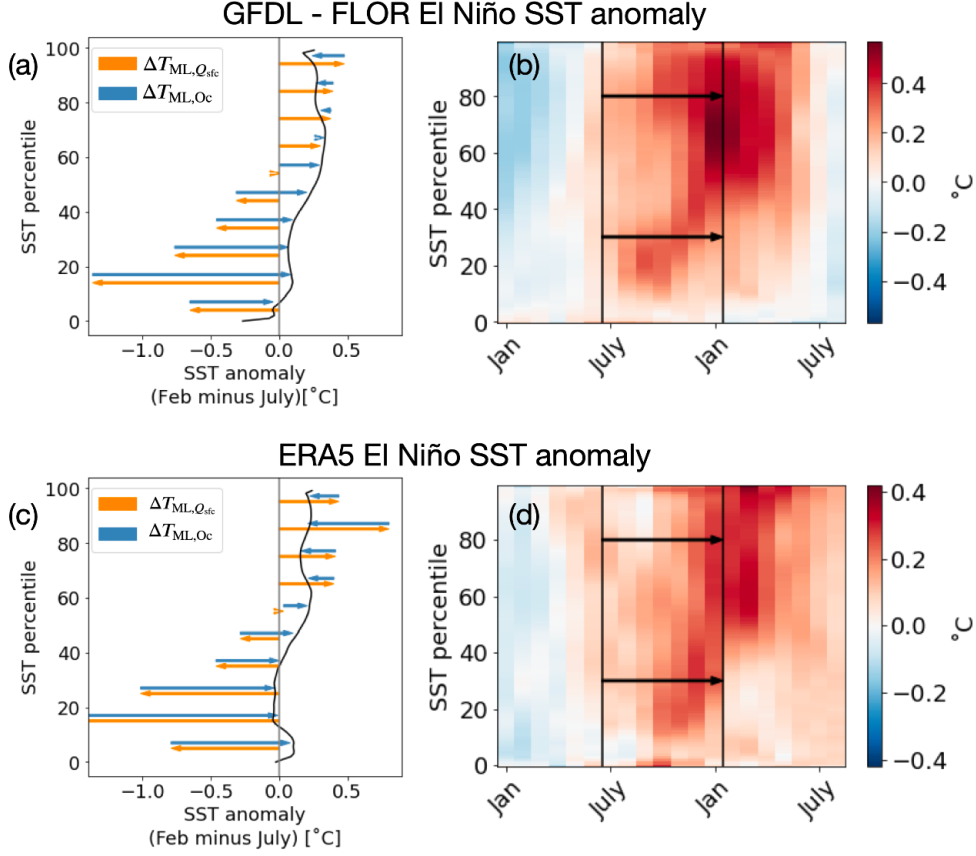


**Figure 2.** Contributions to ocean mixed-layer temperature increase during El Niño. (a, c)  $\Delta T_{ML}$  ( $\approx \Delta SST$ ) at each percentile bin in the global tropics (30S:30N).  $\Delta T_{ML,Q_{sfc}}$  is represented by orange arrows and  $\Delta T_{ML,Oc}$  by blue arrows (calculated as a residual), both averaged over deciles (0-9<sup>th</sup> percentile, 10-19<sup>th</sup> percentile, etc.). (b, d)  $T_{ML}$  anomaly during an El Niño event, composited on the calendar year. Black lines are the limits for the integral represented in (a, c).

175

### 3.2 Latent heat flux anomaly at the warmest SSTs a function of wind speed

176

177

178

179

180

181

At both cold and warm SSTs, the latent heat flux is the largest component of the surface heat flux anomaly (not shown). In order to attribute the latent heat flux ( $\mathcal{L}$ ) anomaly to a surface forcing, in Figure 3 we show the mean El Niño  $\mathcal{L}$  anomaly in SST percentiles, and then separate it into contributions from humidity and wind speed following Equation 3.

182 Consistent with prior studies (W. Wang & McPhaden, 2000; Lloyd et al., 2011),  
 183 we find that the changes in the surface energy budget in the colder 70 percentiles are such  
 184 that the changes in the latent heat flux are following, not forcing, the surface temper-  
 185 ature change. The saturation specific humidity increases when the surface warms but  
 186 the near-surface humidity does not keep up and as a result, the humidity deficit ( $\Delta q$ )  
 187 increases. Changes in the wind speed are overwhelmed by the increase in the humidity  
 188 deficit, so evaporation increases. This is in line with the intuitive expectation of an in-  
 189 crease in evaporation with warming (Eqn. 3, Figure 3b,e).

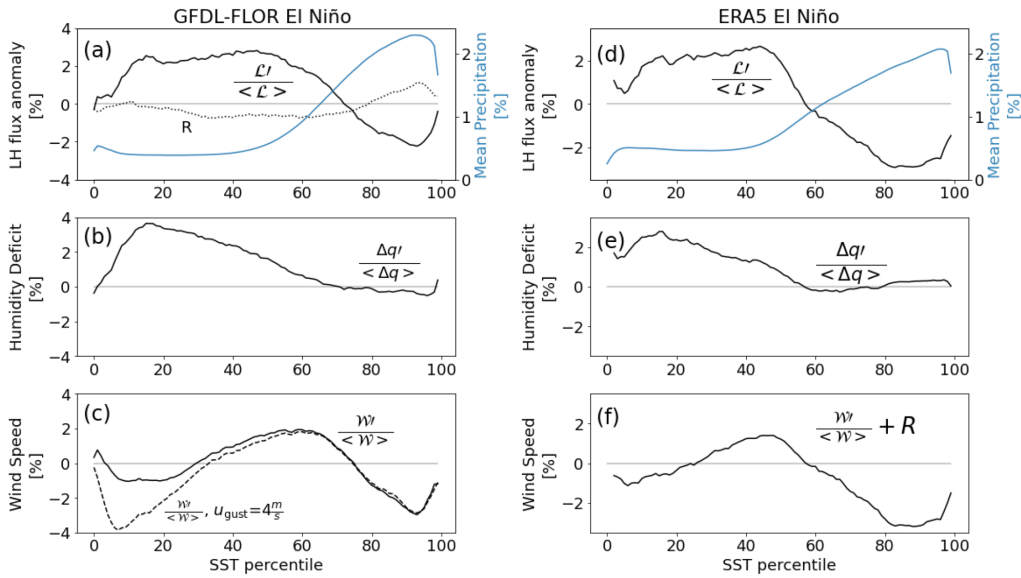


**Figure 3. Contributions to latent heat flux anomaly during El Niño** Top (a, d):  
 Latent heat flux ( $\mathcal{L}$ ) anomaly and mean distribution of precipitation. Middle (b, e): humidity  
 deficit ( $\Delta q$ ) anomaly. Bottom (c, f): anomaly in the surface wind speed  $W$ . Solid lines in (b, c)  
 approximate the solid black line in (a) with the residual  $R$  shown as the dotted line in panel (a)  
 (Equation 3). (c) also shows an estimate of the wind speed anomaly ( $W$ ) if the gustiness ( $u_{\text{gust}}$ )  
 is held constant at  $4\text{ms}^{-1}$ . The wind speed anomaly shown in (f) is estimated as the residual of  
 (d, e). All variables are sorted from coldest to warmest SST.

190 Counter to this intuition,  $\mathcal{L}$  decreases in the warmest 30 percentiles during El Niño  
 191 despite a surface warming (Figure 3a, d, Figure 2). The decrease in  $\mathcal{L}$  accounts for much  
 192 of the decrease in surface heat flux found in Section 3.1.

193 Figure 3(b, c) shows that the humidity deficit at warm SSTs does not change in  
 194 response to El Niño but a decrease in wind speed leads to the decrease in evaporation  
 195 in GFDL-FLOR. The total wind speed  $W$  used for flux calculations in GFDL-FLOR in-  
 196 cludes parameterized sub-grid scale winds we refer to as ‘gustiness,’  $u_{\text{gust}}$  (Beljaars, 1995)  
 197 as well as the winds  $(u, v)$  resolved on the model grid ( $W = \sqrt{u^2 + v^2 + u_{\text{gust}}^2}$ ). We find  
 198 there is very little change in the gustiness during El Niño and the resolved winds drive  
 199 the decrease in wind speed. As a result, the anomaly in the total wind speed  $W$  is well  
 200 approximated by replacing  $u_{\text{gust}}$  with a constant near its mean value (Figure 3c). The  
 201 zonal winds are responsible for the decreased wind speed (not shown), suggesting the weak-  
 202 ened Walker circulation may play a role in forcing the warming of the warmest SSTs.

203 Similarly, in ERA5, there is no anomaly in humidity deficit and instead a reduc-  
 204 tion in wind speed drives the decreased  $\mathcal{L}$  at warm SSTs (Figure 3d, e, f). The ERA5  
 205 dataset also suggests that the zonal winds are the source of the strong negative wind speed  
 206 anomaly in warm percentiles, as found in GFDL-FLOR (not shown).

### 207 **3.3 Positive feedback from longwave radiation**

208 The longwave radiative flux (not shown) is also an important contributor to the  
 209 anomalous surface heat flux at the warmest SSTs, but is a feature of and not a forcing  
 210 for the warming. When the surface and boundary layer warm, the increased downward  
 211 longwave flux from the atmosphere is greater than the increased upward longwave flux  
 212 from the surface. The increased downward longwave flux from the atmosphere is due not  
 213 only to the warming of the atmosphere but also the increased humidity (Allan, 2006).  
 214 The longwave flux anomaly can be explained as a (local) positive feedback, whereas no  
 215 such argument applies to the wind speed. Thus, the change in wind appears to be the  
 216 forcing responsible for the warming at the warmest SSTs.

### 217 **3.4 La Niña parallels El Niño**

218 We find that during the cold phase of ENSO, termed La Niña (S. G. Philander, 1990),  
 219 the same mechanism leads to a cooling in the oceanic regions with deep atmospheric con-  
 220 vection. The cold anomaly at cold SSTs is associated with ocean processes, consistent  
 221 with the expectation that the intensification of the wind-driven upwelling provides a strong  
 222 signal in lower percentiles. On the other hand, surface heat fluxes are responsible for the

223 cold anomaly in the warmest 30 percentiles (Appendix, Figure A1). An increase in sur-  
224 face wind speed, primarily due to meridional winds (not shown), leads to an increase in  
225 evaporation which cools the warmest SSTs (Appendix, Figure A2).

## 226 4 Conclusions

227 The warming of the tropical free troposphere during El Niño is due to a warming  
228 of the surface in regions with atmospheric deep convection. We find the warm SST anomaly  
229 there is not due to local ocean dynamics, but results from a surface heat flux anomaly.  
230 The surface heat flux anomaly can be traced back to a decrease in the surface wind speed  
231 (primarily the zonal component) which damps evaporation. Since the surface wind speed  
232 in the regions with atmospheric deep convection is lower during El Niño than in the cli-  
233 matic base state, the highest SSTs in the El Niño state are higher than in the base state,  
234 leading to the prominent atmospheric warming.

235 The results presented here may also have ramifications for theory and idealized mod-  
236 eling of ocean-atmosphere coupling. We have shown that the latent heat flux over trop-  
237 ical oceans does not vary as a function of SST alone, although it has been parameter-  
238 ized as such in simple models of tropical Pacific SST variability, including models of the  
239 response to anthropogenic forcing (Seager et al., 1988, 2019; Vialard et al., 2001).

240 The wind-forced ocean heat uptake anomaly in the warm regions partially opposes  
241 the heat flux anomaly in the upwelling regions, where oceanic heat uptake is reduced (W. Wang  
242 & McPhaden, 2000; Trenberth et al., 2002; Lloyd et al., 2011). This interplay between  
243 heat uptake in colder and warmer parts of the tropics may also affect longer-term vari-  
244 ations in ocean heat uptake and temperature trends (Watanabe et al., 2020; Po-Chedley  
245 et al., 2021). Future work will investigate its role in decadal modes such as the Inter-  
246 decadal Pacific Oscillation, the primary mode of decadal climate variability in the Pa-  
247 cific Ocean, which may contribute to variations in the global mean surface temperature  
248 that are caused by changes to the rate of ocean heat uptake (Xie et al., 2016).

## 249 Acknowledgments

250 A.K.H. acknowledges support from the National Science Foundation Graduate Re-  
251 search Fellowship Program under Grant No. DGE-2039656. Any opinions, findings, and  
252 conclusions or recommendations expressed in this material are those of the author and

253 do not necessarily reflect the views of the National Science Foundation. The authors thank  
254 Wenchang Yang for making available the FLOR pre-industrial control experiment (Yang  
255 et al., 2019). ERA5 data was downloaded from the Copernicus Climate Data Store in  
256 January 2020 (Hersbach et al., 2019). The FLOR result used in this study is hosted by  
257 Dataspace (<https://doi.org/10.34770/g7fe-hs07>). The authors declare no competing fi-  
258 nancial interests.

## 259 References

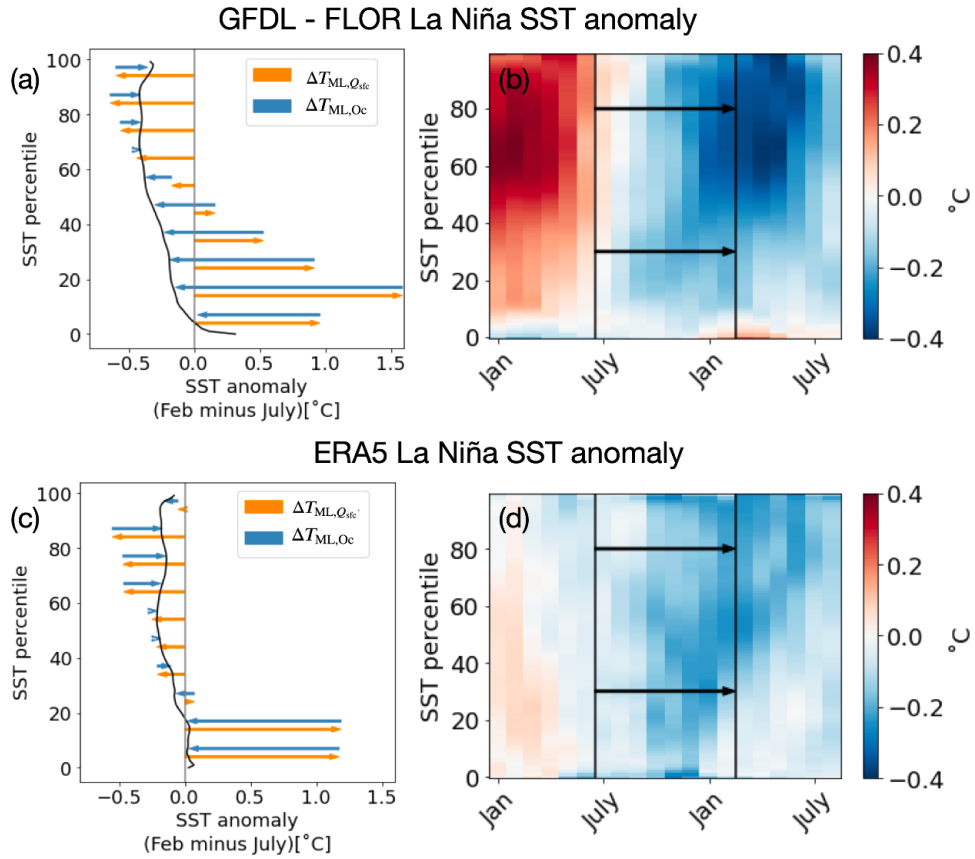
- 260 Alexander, M. A., Bladé, I., Newman, M., Lanzante, J. R., Lau, N.-C., & Scott,  
261 J. D. (2002). The atmospheric bridge: The influence of enso teleconnections  
262 on air–sea interaction over the global oceans. *Journal of climate*, *15*(16),  
263 2205–2231.
- 264 Allan, R. P. (2006). Variability in clear-sky longwave radiative cooling of the atmo-  
265 sphere. *Journal of Geophysical Research*, *111*. doi: 10.1029/2006JD007304
- 266 Beljaars, A. C. (1995). The parametrization of surface fluxes in large-scale models  
267 under free convection. *Quarterly Journal of the Royal Meteorological Society*,  
268 *121*(522), 255–270.
- 269 Bjercknes, J. (1969). Atmospheric teleconnections from the equatorial pacific.  
270 *Monthly weather review*, *97*(3), 163–172.
- 271 Brown, R. G., & Bretherton, C. S. (1997). A test of the strict quasi-equilibrium the-  
272 ory on long time and space scales. *Journal of the Atmospheric Sciences*, *54*(5),  
273 624–638. doi: 10.1175/1520-0469(1997)054<0624:ATOTSQ>2.0.CO;2
- 274 Chiang, J. C. H., & Sobel, A. H. (2002). Tropical tropospheric temperature vari-  
275 ations caused by ENSO and their influence on the remote tropical climate\*.  
276 *Journal of Climate*, *15*(18), 2616–2631. doi: 10.1175/1520-0442(2002)015<2616:  
277 TTTVCB>2.0.CO;2
- 278 Delworth, T. L., Broccoli, A. J., Rosati, A., Stouffer, R. J., Balaji, V., Beesley, J. A.,  
279 ... Zhang, R. (2006). GFDL’s CM2 global coupled climate models. part i:  
280 Formulation and simulation characteristics. *Journal of Climate*, *19*(5), 643–  
281 674. doi: 10.1175/JCLI3629.1
- 282 Delworth, T. L., Rosati, A., Anderson, W., Adcroft, A. J., Balaji, V., Benson, R., ...  
283 Zhang, R. (2012). Simulated climate and climate change in the GFDL CM2.5  
284 high-resolution coupled climate model. *Journal of Climate*, *25*(8), 2755–2781.

- 285 doi: 10.1175/JCLI-D-11-00316.1
- 286 Fueglistaler, S. (2019). Observational evidence for two modes of coupling between  
287 sea surface temperatures, tropospheric temperature profile, and shortwave  
288 cloud radiative effect in the tropics. *Geophysical Research Letters*, *46*(16),  
289 9890–9898. doi: 10.1029/2019GL083990
- 290 Graham, N. E., & Barnett, T. P. (1987). Sea surface temperature, surface wind di-  
291 vergence, and convection over tropical oceans. *Science*, *238*(4827), 657–659.
- 292 Hersbach, H., Bell, B., Berrisford, P., Biavati, G., Horányi, A., Muñoz Sabater, J.,  
293 ... others (2019). Era5 monthly averaged data on single levels from 1979 to  
294 present. *Copernicus Climate Change Service (C3S) Climate Data Store (CDS)*,  
295 *10*.
- 296 Klein, S. A., Soden, B. J., & Lau, N.-C. (1999). Remote sea surface temperature  
297 variations during ENSO: Evidence for a tropical atmospheric bridge. *Journal*  
298 *of Climate*, *12*(4), 917–932. doi: 10.1175/1520-0442(1999)012<0917:RSSTVD>2  
299 .0.CO;2
- 300 Large, W. G., & Yeager, S. G. (2009). The global climatology of an interannually  
301 varying air–sea flux data set. *Climate Dynamics*, *33*(2), 341–364. doi: 10.1007/  
302 s00382-008-0441-3
- 303 Lau, N.-C., & Nath, M. J. (1996). The role of the “atmospheric bridge” in linking  
304 tropical pacific enso events to extratropical sst anomalies. *Journal of Climate*,  
305 *9*(9), 2036–2057.
- 306 Lintner, B. R., & Chiang, J. C. H. (2005). Reorganization of tropical climate during  
307 el niño: A weak temperature gradient approach. *Journal of Climate*, *18*(24),  
308 5312–5329. doi: 10.1175/JCLI3580.1
- 309 Lloyd, J., Guilyardi, E., & Weller, H. (2011). The role of atmosphere feedbacks  
310 during ENSO in the CMIP3 models. part II: using AMIP runs to understand  
311 the heat flux feedback mechanisms. *Climate Dynamics*, *37*(7), 1271–1292. doi:  
312 10.1007/s00382-010-0895-y
- 313 Lohmann, K., & Latif, M. (2007). Influence of el niño on the upper-ocean circulation  
314 in the tropical atlantic ocean. *Journal of Climate*, *20*(19), 5012–5018. doi: 10  
315 .1175/JCLI4292.1
- 316 Lu, J., Chen, G., & Frierson, D. M. W. (2008). Response of the zonal mean at-  
317 mospheric circulation to el niño versus global warming. *Journal of Climate*,

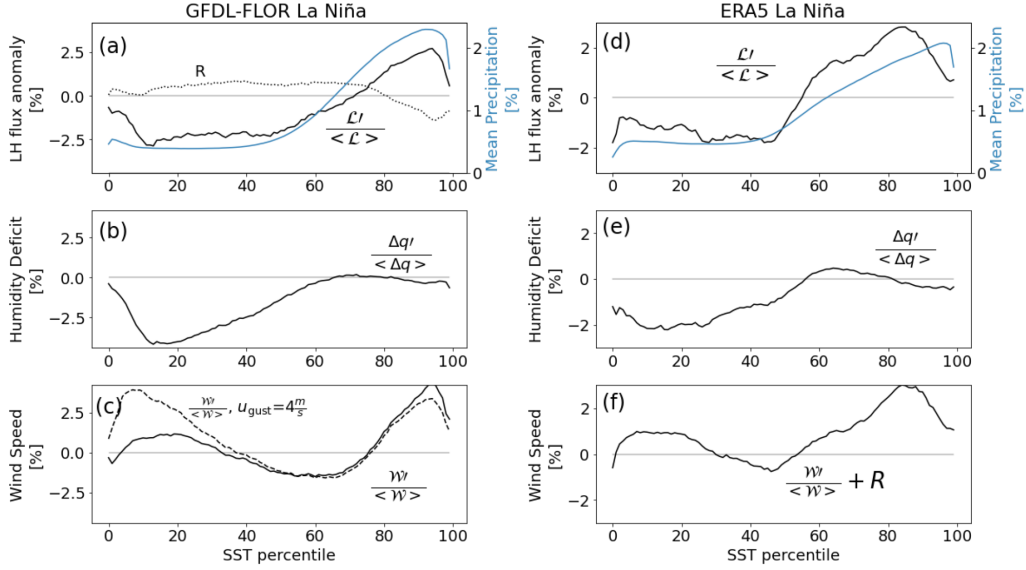
- 318           21 (22), 5835–5851. doi: 10.1175/2008JCLI2200.1
- 319 Milly, P. C., Malyshev, S. L., Shevliakova, E., Dunne, K. A., Findell, K. L., Gleeson,  
320 T., . . . Swenson, S. (2014). An enhanced model of land water and energy  
321 for global hydrologic and earth-system studies. *Journal of Hydrometeorology*,  
322 15(5), 1739–1761.
- 323 Philander, S. G. (1990). El niño, la niña, and the southern oscillation. *International*  
324 *Geophysics Series*, 46, 9–11.
- 325 Philander, S. G. H. (1983). El niño southern oscillation phenomena. *Nature*,  
326 302(5906), 295–301. doi: 10.1038/302295a0
- 327 Po-Chedley, S., Santer, B. D., Fueglistaler, S., Zelinka, M. D., Cameron-Smith,  
328 P. J., Painter, J. F., & Fu, Q. (2021). Natural variability contributes to  
329 model–satellite differences in tropical tropospheric warming. *Proc. Nat. Acad.*  
330 *of Sciences*, 118(13), e2020962118. doi: 10.1073/pnas.2020962118
- 331 Rasmusson, E. M., & Wallace, J. M. (1983). Meteorological aspects of the el  
332 niño/southern oscillation. *Science*, 222(4629), 1195–1202.
- 333 Seager, R., Cane, M., Henderson, N., Lee, D.-E., Abernathey, R., & Zhang, H.  
334 (2019). Strengthening tropical pacific zonal sea surface temperature gradi-  
335 ent consistent with rising greenhouse gases. *Nature Climate Change*, 9(7),  
336 517–522. doi: 10.1038/s41558-019-0505-x
- 337 Seager, R., Harnik, N., Kushnir, Y., Robinson, W., & Miller, J. (2003). Mechanisms  
338 of hemispherically symmetric climate variability. *Journal of Climate*, 16(18),  
339 2960–2978. doi: 10.1175/1520-0442(2003)016<2960:MOHSCV>2.0.CO;2
- 340 Seager, R., Zebiak, S. E., & Cane, M. A. (1988). A model of the tropical pacific sea  
341 surface temperature climatology. *Journal of Geophysical Research: Oceans*, 93,  
342 1265–1280. doi: <https://doi.org/10.1029/JC093iC02p01265>
- 343 Sobel, A. H., Held, I. M., & Bretherton, C. S. (2002). The ENSO signal in tropi-  
344 cal tropospheric temperature. *Journal of Climate*, 15(18), 2702–2706. doi: 10  
345 .1175/1520-0442(2002)015<2702:TESITT>2.0.CO;2
- 346 Trenberth, K. E. (1997). The definition of el niño. *Bulletin of the American Me-*  
347 *teorological Society*, 78(12), 2771–2777. doi: 10.1175/1520-0477(1997)078<2771:  
348 TDOENO>2.0.CO;2
- 349 Trenberth, K. E. (2002). Evolution of el niño–southern oscillation and global atmo-  
350 spheric surface temperatures. *Journal of Geophysical Research*, 107. doi: 10

- 351 .1029/2000JD000298
- 352 Trenberth, K. E., Stepaniak, D. P., & Caron, J. M. (2002). Interannual variations in  
353 the atmospheric heat budget. *Journal of Geophysical Research*, *107*. doi: 10  
354 .1029/2000JD000297
- 355 Vecchi, G. A., Delworth, T., Gudgel, R., Kapnick, S., Rosati, A., Wittenberg,  
356 A. T., ... Zhang, S. (2014). On the seasonal forecasting of regional  
357 tropical cyclone activity. *Journal of Climate*, *27*(21), 7994–8016. doi:  
358 10.1175/JCLI-D-14-00158.1
- 359 Vialard, J., Menkes, C., Boulanger, J.-P., Delecluse, P., Guilyardi, E., McPhaden,  
360 M. J., & Madec, G. (2001). A model study of oceanic mechanisms af-  
361 fecting equatorial pacific sea surface temperature during the 1997–98 el  
362 niño. *Journal of Physical Oceanography*, *31*(7), 1649–1675. doi: 10.1175/  
363 1520-0485(2001)031<1649:AMSOOM>2.0.CO;2
- 364 Wang, B. (1995). Transition from a cold to a warm state of the el niño-southern os-  
365 cillation cycle. *Meteorology and Atmospheric Physics*, *56*(1), 17–32.
- 366 Wang, W., & McPhaden, M. J. (2000). The surface-layer heat balance in the equato-  
367 rial pacific ocean. part II: Interannual variability. *Journal of Physical Oceanog-  
368 raphy*, *30*(11), 2989–3008. doi: 10.1175/1520-0485(2001)031<2989:TSLHBI>2.0  
369 .CO;2
- 370 Watanabe, M., Dufresne, J. L., Kosaka, Y., Mauritsen, T., & Tatebe, H. (2020).  
371 Enhanced warming constrained by past trends in equatorial pacific sea surface  
372 temperature gradient. *Nat. Clim. Change*, *11*, 33–37.
- 373 Xie, S.-P., Kosaka, Y., & Okumura, Y. M. (2016). Distinct energy budgets for an-  
374 thropogenic and natural changes during global warming hiatus. *Nature Geo-  
375 science*, *9*(1), 29–33. doi: 10.1038/ngeo2581
- 376 Yang, W., Vecchi, G. A., Fueglistaler, S., Horowitz, L. W., Luet, D. J., Muñoz,  
377 Á. G., ... Underwood, S. (2019). Climate impacts from large volcanic erup-  
378 tions in a high-resolution climate model: The importance of forcing structure.  
379 *Geophysical Research Letters*, *46*(13), 7690–7699.
- 380 Yulaeva, E., & Wallace, J. (1994). The signature of ENSO in global temperature  
381 and precipitation fields derived from the microwave sounding unit. *Journal of  
382 Climate*.

## Appendix A Supplemental Figures



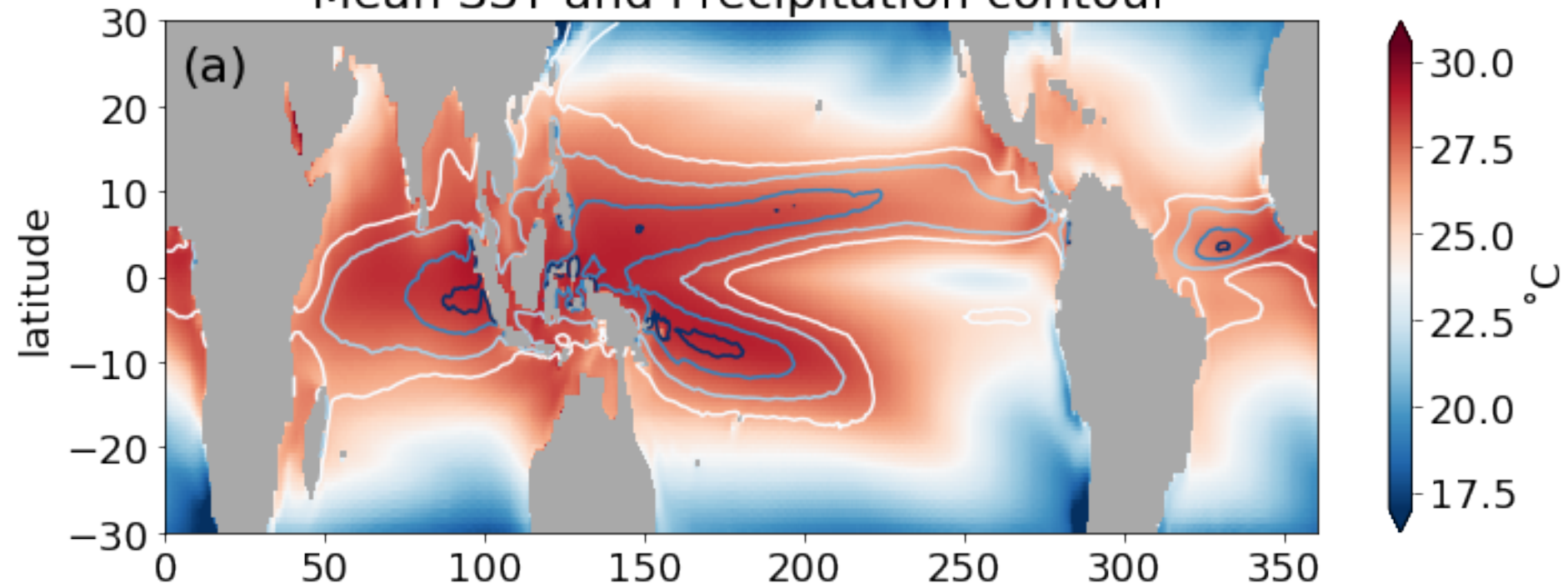
**Figure A1.** Contributions to ocean mixed-layer temperature decrease during La Niña. (a, c)  $\Delta T_{ML}$  ( $\approx \Delta SST$ ) at each percentile bin in the global tropics (30S:30N).  $\Delta T_{ML,Q_{sfc}}$  is represented by orange arrows and  $\Delta T_{ML,Oc}$  by blue arrows (calculated as a residual), both averaged over deciles (0-9<sup>th</sup> percentile, 10-19<sup>th</sup> percentile, etc.). (b, d)  $T_{ML}$  anomaly during a La Niña event, composited on the calendar year. Black lines are the limits for the integral represented in (a, c).



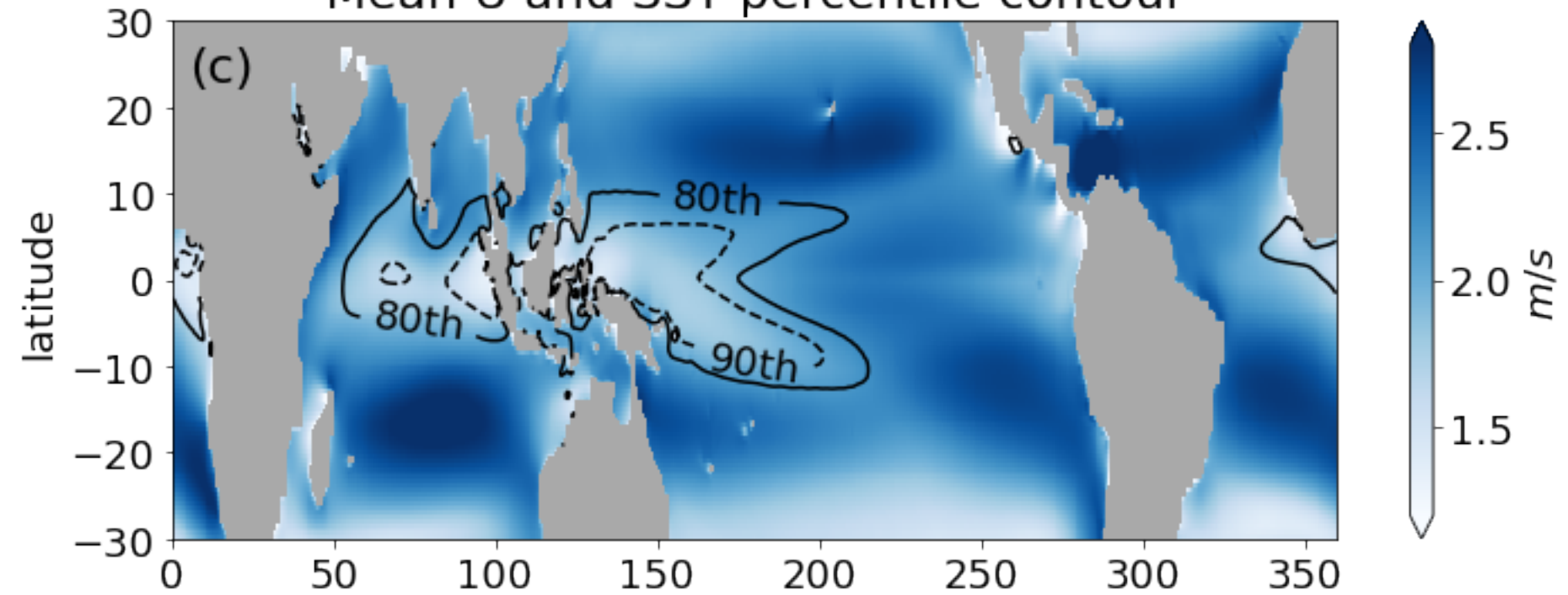
**Figure A2.** Latent heat flux anomaly during La Niña as a fraction of its climatological value. Top (a, d):  $\mathcal{L}$  anomaly and mean distribution of precipitation. Middle (b, e): humidity deficit  $\Delta q$  anomaly. Bottom (c, f): anomaly in the surface wind speed  $W$ . Solid lines in (b, c) approximate the solid black line in (a) with the residual  $R$  shown as the dotted line in panel (a) (Equation 3). (c) also shows an estimate of  $W$  if the gust speed is held constant at  $4\text{ms}^{-1}$ . The wind speed anomaly shown in (f) is estimated as the residual of (d, e). All variables are sorted from coldest to warmest SST.

Figure 1.

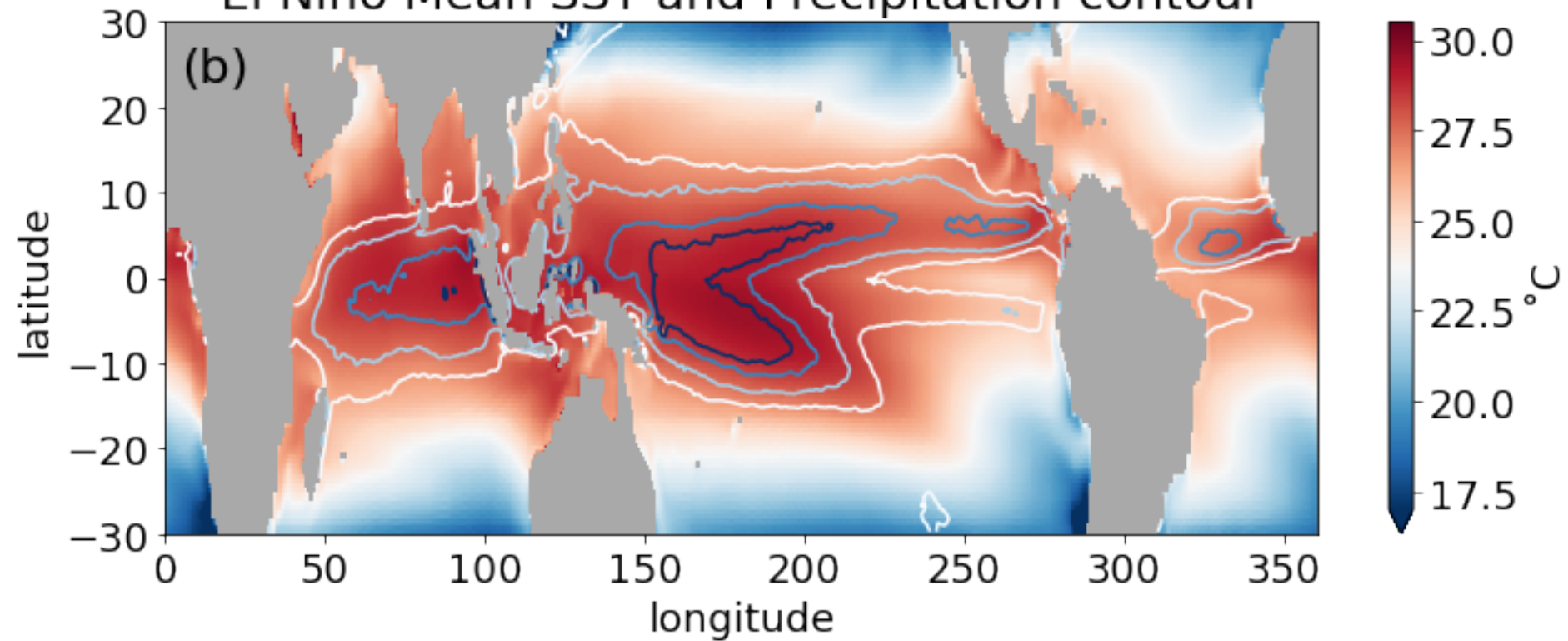
Mean SST and Precipitation contour



Mean U and SST percentile contour



El Niño Mean SST and Precipitation contour



El Niño U and SST percentile contour

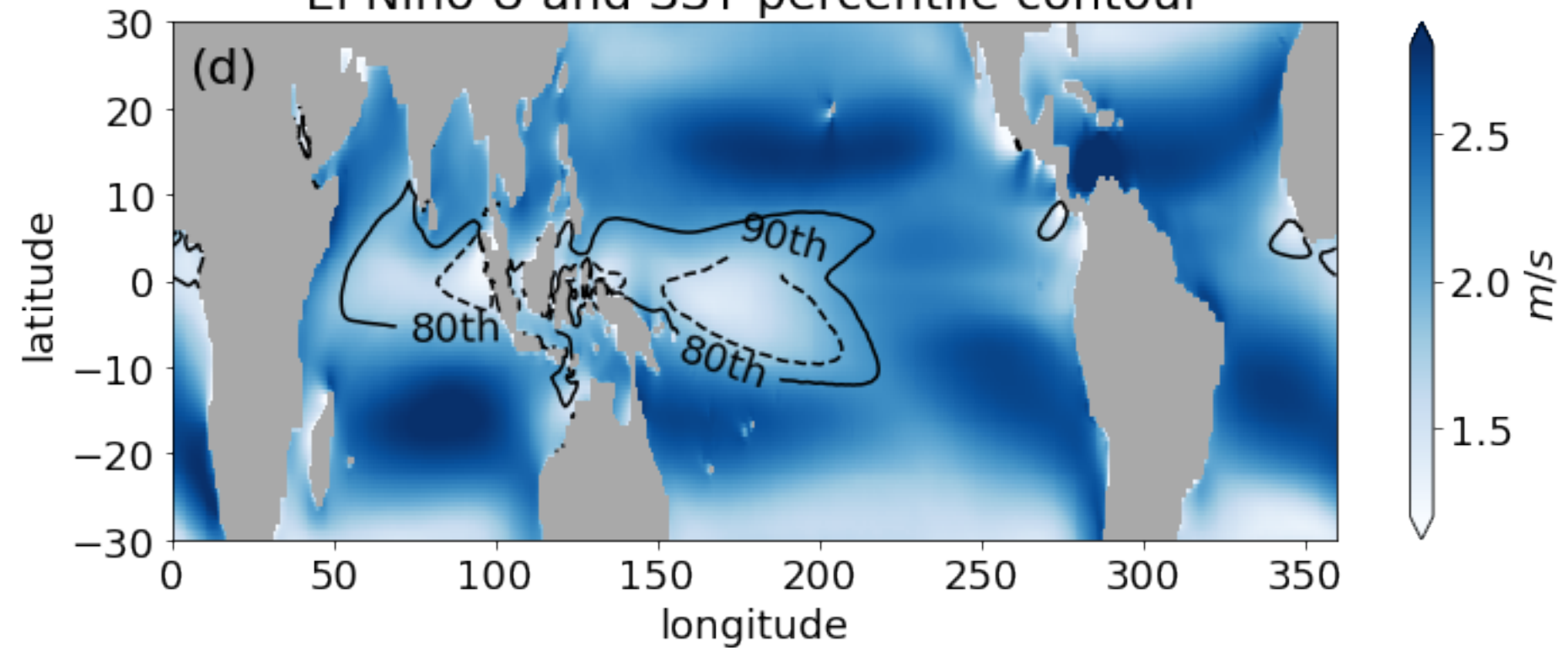
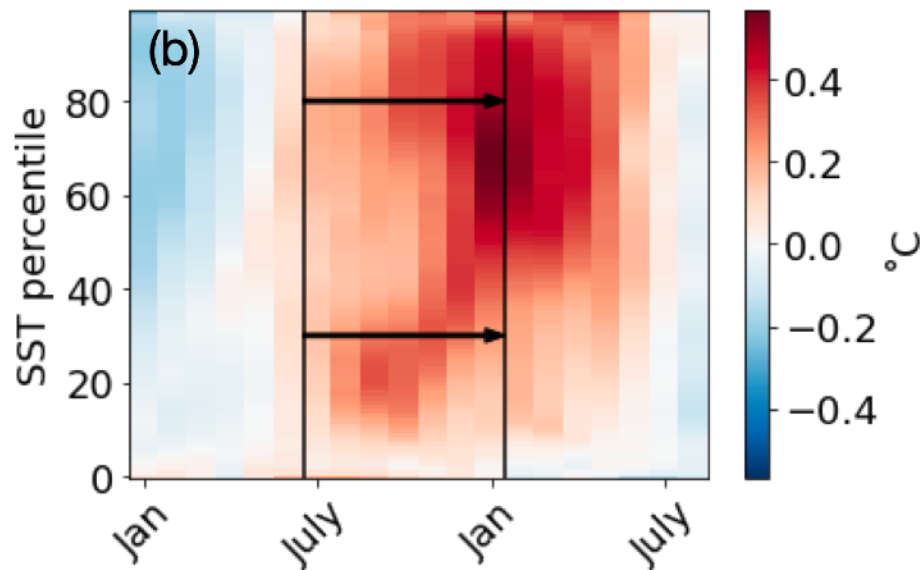
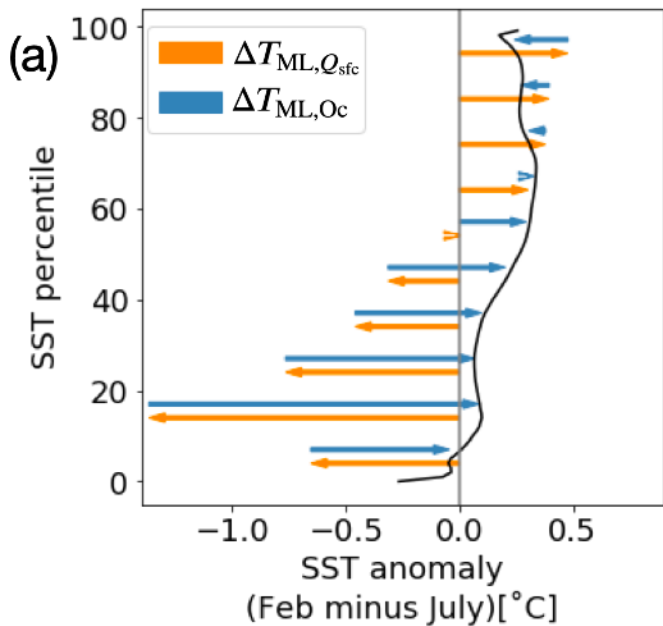


Figure 2.

# GFDL - FLOR El Niño SST anomaly



# ERA5 El Niño SST anomaly

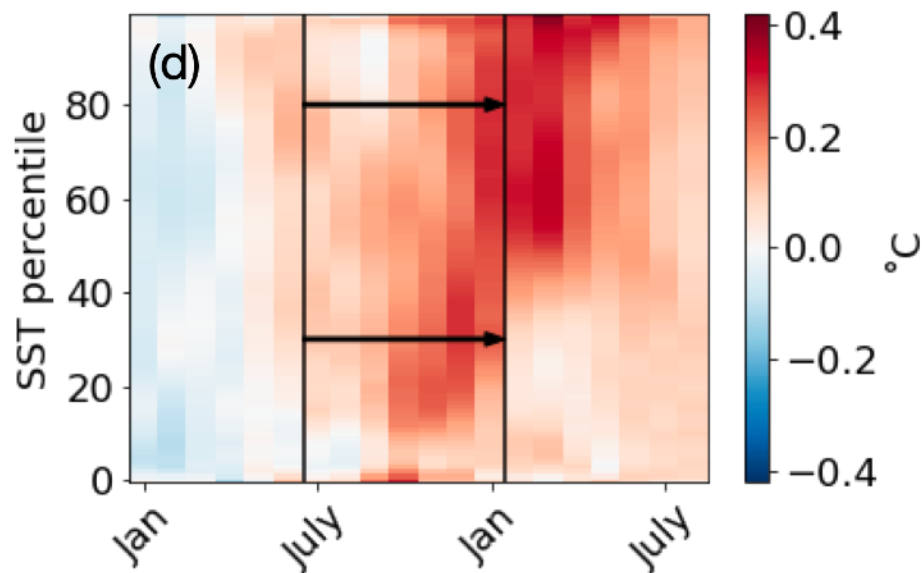
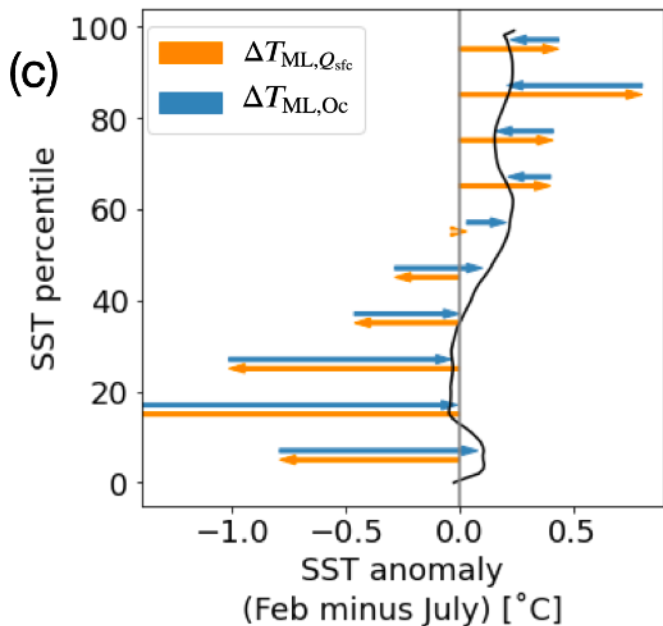
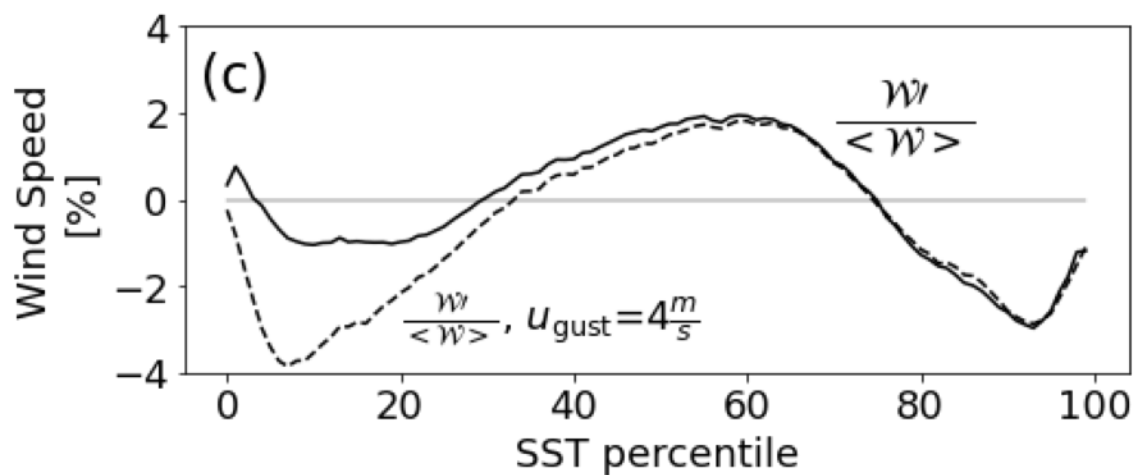
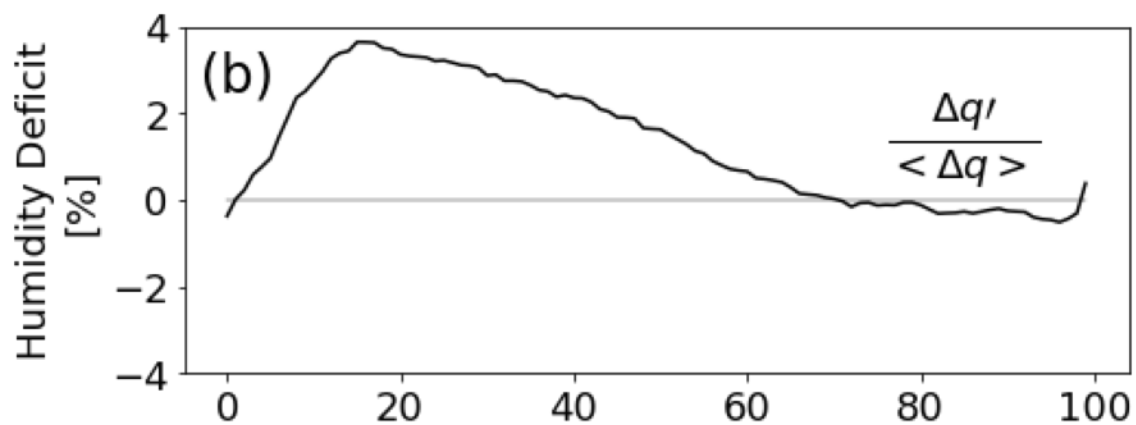
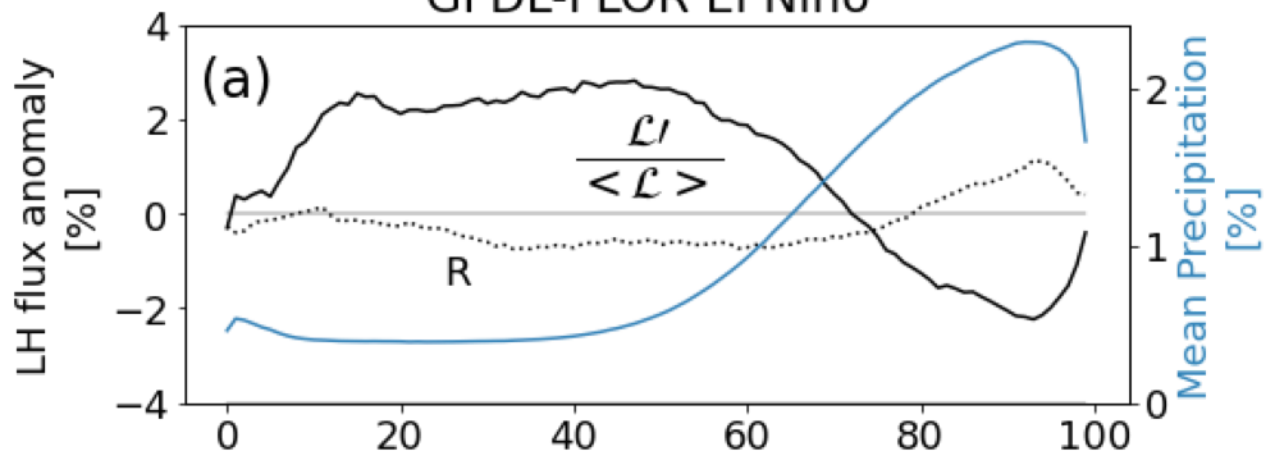


Figure 3.

GFDL-FLOR El Niño



ERA5 El Niño

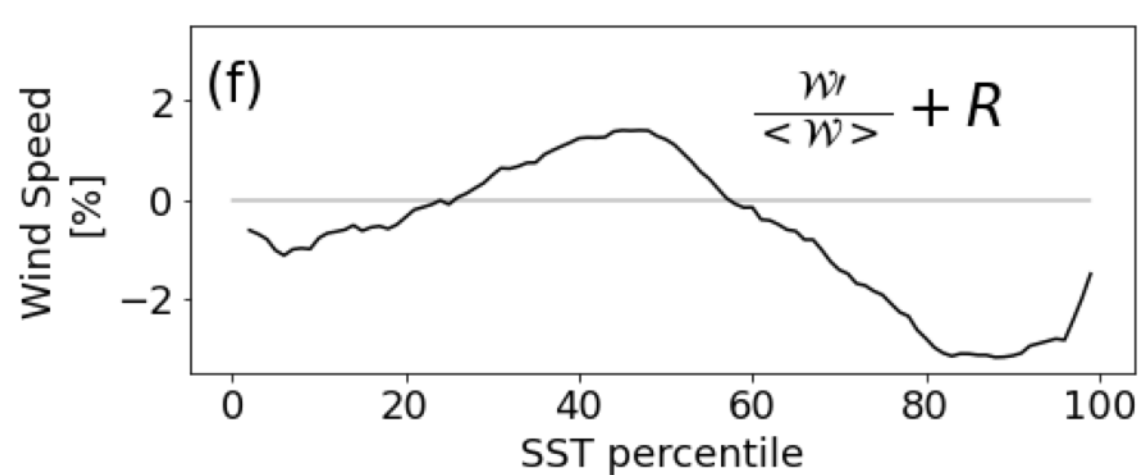
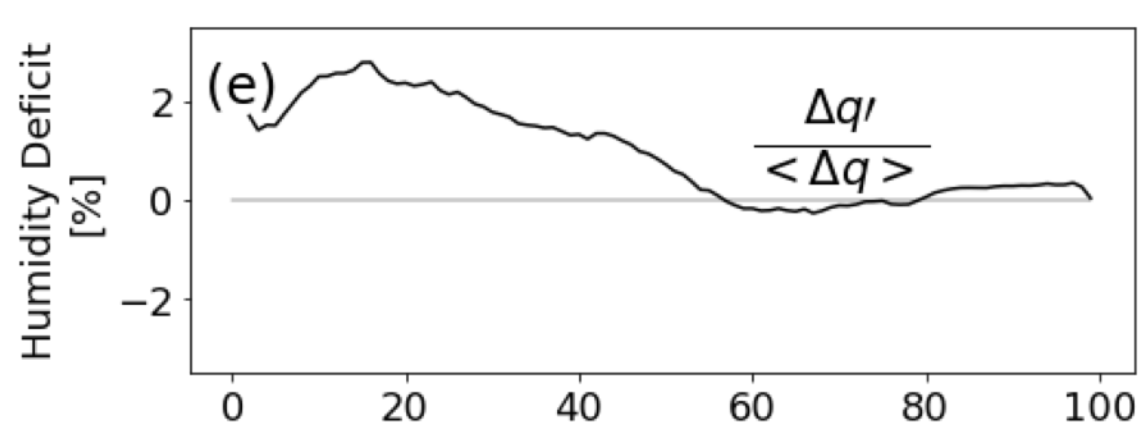
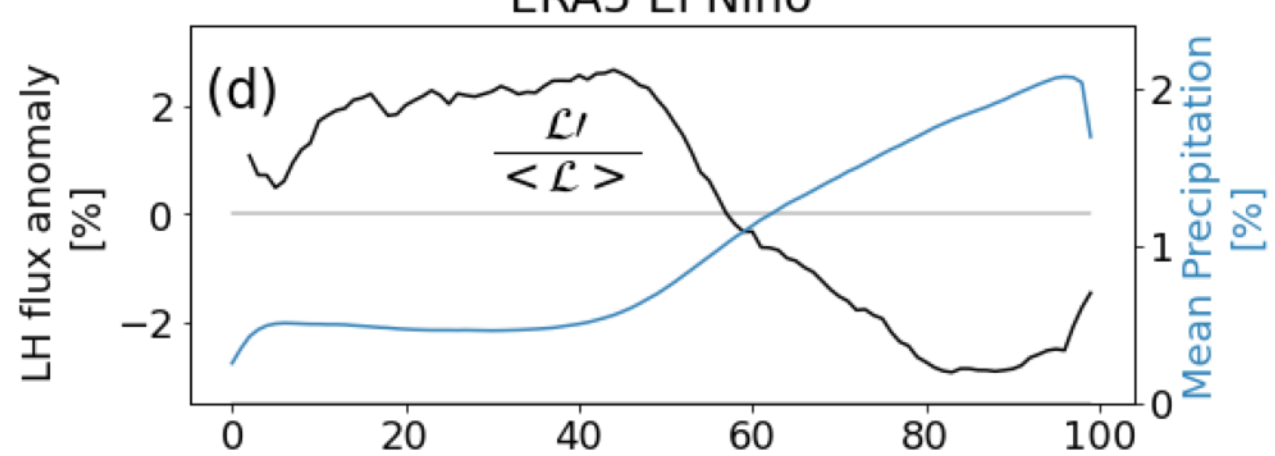
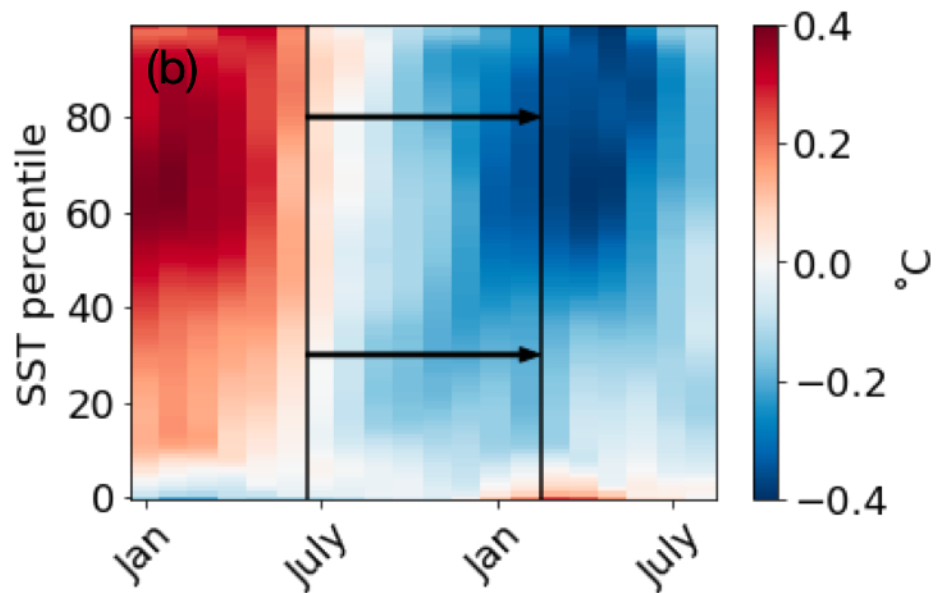
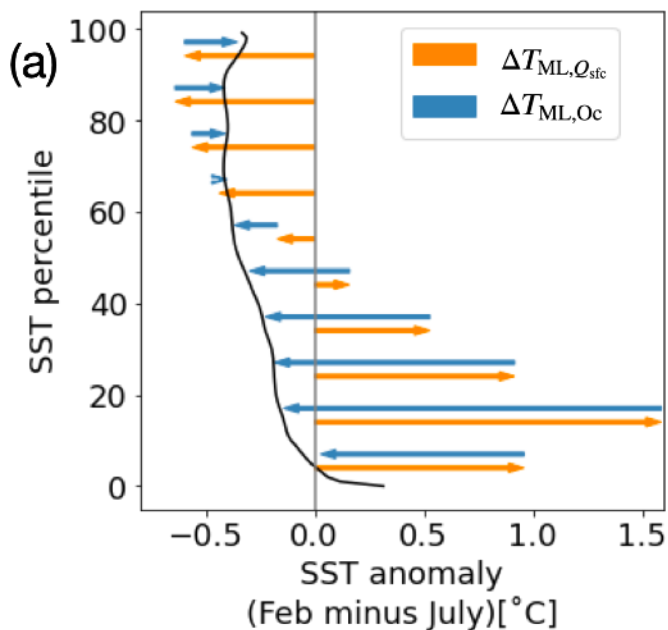


Figure A1.

## GFDL - FLOR La Niña SST anomaly



## ERA5 La Niña SST anomaly

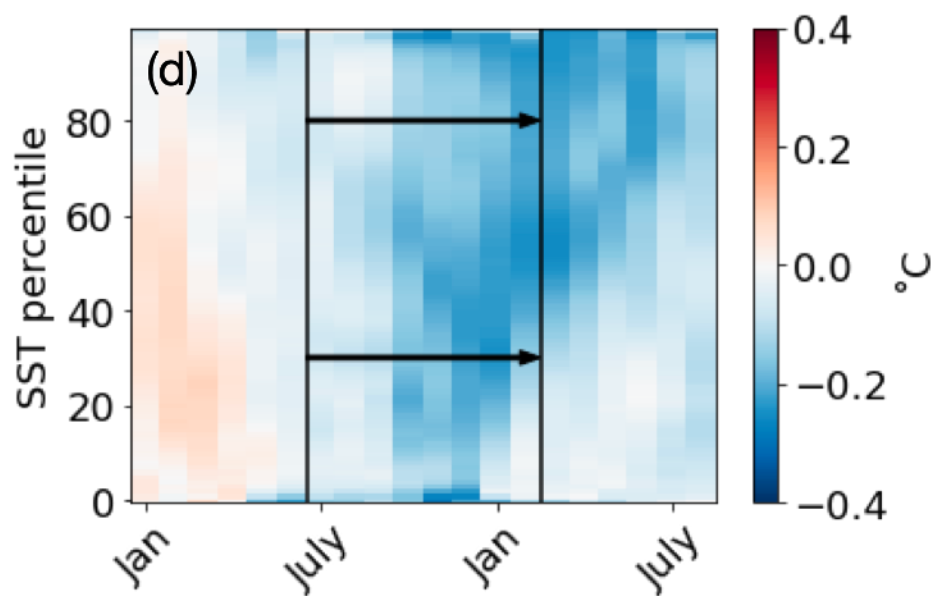
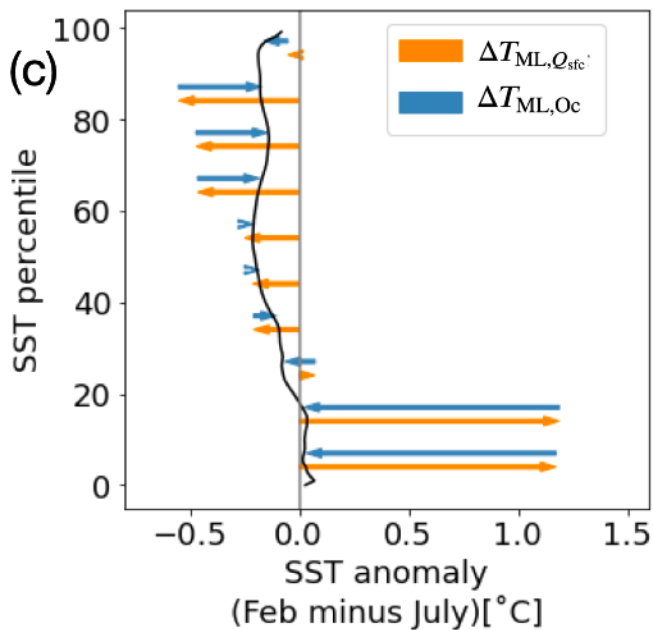
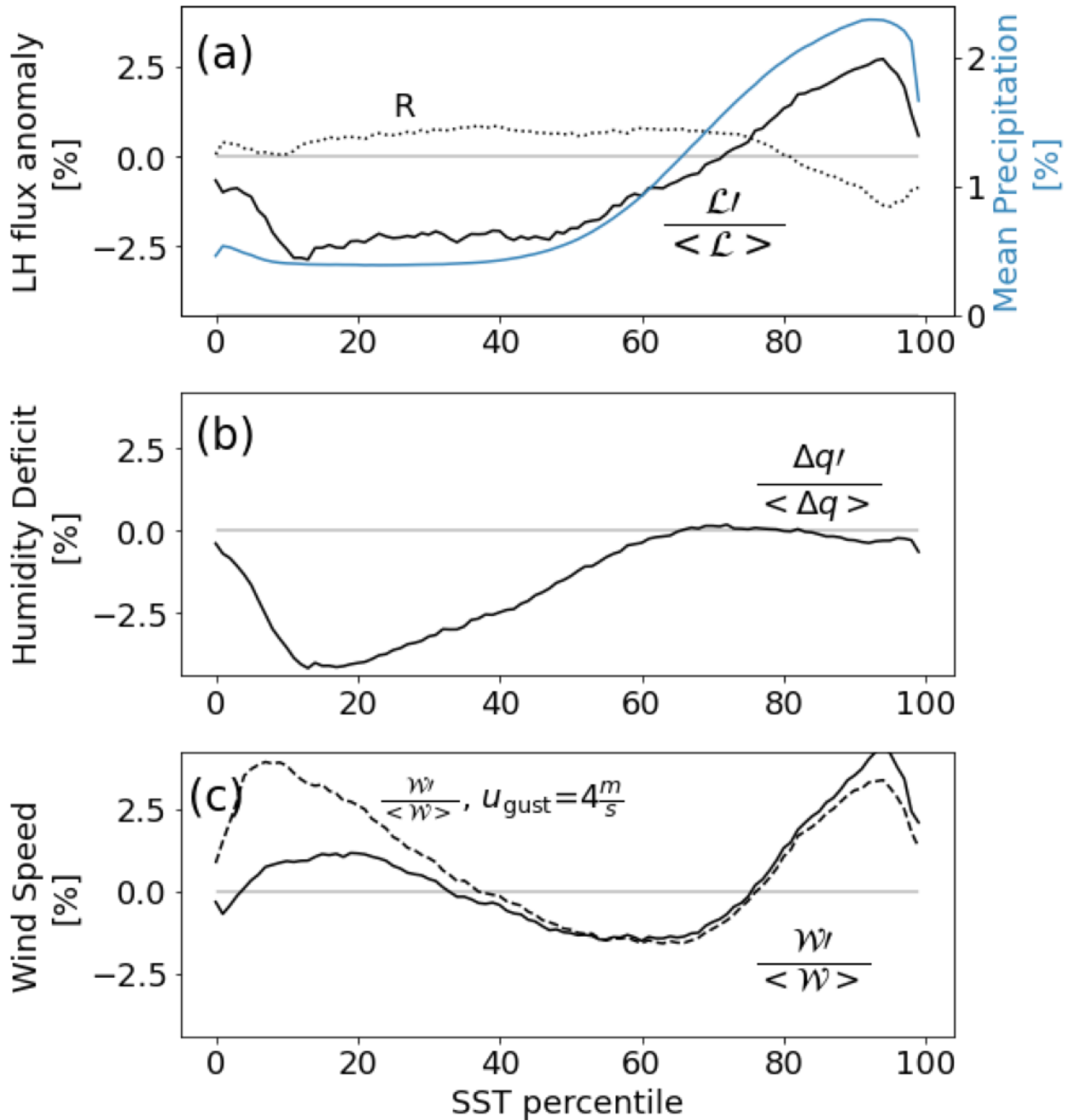


Figure A2.

GFDL-FLOR La Niña



ERA5 La Niña

